

Successive Partial Disruptions with Orbital Precession in a White Dwarf–Black Hole System for Repeating GRB 250702B

YURI SATO ,¹ RIN OIKAWA ,¹ KAZUMA KATO,¹ TATSUYA MATSUMOTO ,² AND KAZUMI KASHIYAMA ¹

¹ *Astronomical Institute, Graduate School of Science, Tohoku University, Sendai 980-8578, Japan*

² *Department of Astronomy, School of Science, The University of Tokyo, 7-3-1 Hongo, Bunkyo-ku, Tokyo 113-0033, Japan*

ABSTRACT

The peculiar gamma-ray burst GRB 250702B is the longest event ever observed, lasting about one day and exhibiting four prompt-emission flares of ~ 100 s with irregular recurrence intervals of at least one hour. To explain this hierarchy of timescales, we consider a scenario in which a stellar object undergoes repeated partial tidal disruptions by a black hole (BH). We find that if a white dwarf (WD) is on a highly eccentric orbit ($e \approx 0.97$) around an intermediate-mass black hole (BH) with $M_{\text{BH}} \lesssim 10^6 M_{\odot}$ and $a = 50 R_{\odot} (M_{\text{BH}}/10^6 M_{\odot})^{1/3}$, the observed properties of GRB 250702B can be naturally reproduced. In this framework, the duration of each flare is determined by the viscous accretion timescale of material stripped near pericenter, with a typical mass $\Delta M \approx 2 \times 10^{-2} M_{\odot}$. The minimum recurrence time corresponds to the orbital period, while the total activity period is set by the secular orbital evolution timescale leading to the complete disruption of the WD. Furthermore, if $M_{\text{BH}} \gtrsim 10^5 M_{\odot}$ and the orbit has a minimum polar angle relative to the BH equatorial plane of $\theta_{\text{min}} \gtrsim 0.12$ rad, relativistic frame dragging induces $\gtrsim 0.1$ rad precession of the orbital angular momentum between successive pericenter passages, comparable to a typical GRB jet half-opening angle, resulting in intermittent alignment with the observer and irregular flare spacing. The WD experiences ≈ 40 jet-launch episodes before complete disruption, but only four are expected to be observed on-axis. The remaining off-axis jets become visible at late times, enhancing the radio afterglow by about an order of magnitude, providing a testable prediction of this scenario.

Keywords: Gamma-ray bursts (629) – Tidal disruption (1696)

1. INTRODUCTION

Recently, an exceptionally long-duration gamma-ray burst, GRB 250702B, was detected, exhibiting the longest prompt emission duration ever observed (E. Neights et al. 2025). The event was first discovered by the *Einstein Probe* (EP) in X-rays (D. Y. Li et al. 2025) and was subsequently detected by the *Fermi* Gamma-ray Burst Monitor (*Fermi*/GBM) about one day later (E. Neights et al. 2025). The first gamma-ray flare occurred approximately 10 hours after the initial X-ray detection, followed by several subsequent flares with irregular separations ranging from ~ 1 to ~ 25 hours (D. Y. Li et al. 2025; J.-P. Zhang et al. 2025; G. Oganesyan et al. 2025; E. Neights et al. 2025). Each flare lasts for $\delta t_{\text{flare}} \sim 100$ s. The total activity duration reached $\delta t_{\text{tot}} \sim 1.6$ d, with an isotropic-equivalent luminosity of

$L_{\gamma, \text{iso}} \approx 5 \times 10^{51}$ erg s⁻¹ at $z = 1.036$ (B. P. Gompertz et al. 2025). Multiwavelength follow-up observations detected X-ray, infrared, and radio emission (A. J. Levan et al. 2025; J. Carney et al. 2025; B. O’Connor et al. 2025), and the transient was localized at an offset of 5.7 kpc from the center of its host galaxy (J. Carney et al. 2025).

The coexistence of short (~ 100 s) flares, irregular hour-scale recurrence, and prolonged day-scale activity makes GRB 250702B highly unusual among known GRBs, suggesting a physical origin distinct from both compact-object mergers and collapsars. Such hierarchical timescales have been proposed to arise in tidal disruption events (TDEs) (A. J. Levan et al. 2025; P. Beniamini et al. 2025; R. A. Eyles-Ferris et al. 2025; D. Y. Li et al. 2025; J. Granot et al. 2025).

A similar phenomenology was observed in the first known jetted TDE, Swift J1644+57, which showed multiple high-energy flares separated by \sim day-long inter-

vals, while individual flares rose on ~ 100 s timescales (D. N. Burrows et al. 2011; A. J. Levan et al. 2011). These timescales have been interpreted in a white dwarf–intermediate-mass black hole (WD–IMBH) disruption scenario, in which the short timescale reflects the accretion time, and the longer one corresponds to the orbital period of the WD (J. H. Krolik & T. Piran 2011). In contrast, GRB 250702B exhibits flares recurring at irregular intervals as short as $\Delta t_{\text{flare,min}} \sim 1$ hour, while the flare durations remain comparable. This hierarchy points to a more compact system in which the WD survives multiple close encounters with the BH, as expected for partial tidal disruptions (e.g., I. Zalamea et al. 2010; M. MacLeod et al. 2014; J.-H. Chen et al. 2023; S. Y. Lau & H. Yu 2025; J.-P. Chen et al. 2025).

In this Letter, we propose that the temporal hierarchy of GRB 250702B arises from successive partial tidal disruptions of the WD orbiting the BH. If the WD approaches sufficiently close to the BH, frame dragging induces relativistic precession of its orbit. At each pericenter passage, a fraction of the WD is stripped and circularizes into a transient accretion disk, launching a relativistic jet. Orbital precession causes the jet-launching direction to vary between passages, so that most jets are viewed off-axis, with only a few aligning with the observer’s line of sight and producing detectable prompt gamma-ray flares. This framework will explain the co-existence of short-duration flares, irregular recurrence, and prolonged activity in GRB 250702B, and predicts enhanced late-time radio emission from the cumulative contribution of multiple off-axis jets.

2. PHYSICAL PICTURE AND TIMESCALE HIERARCHY

2.1. Repeating Partial Disruptions

We consider a scenario in which a WD of mass M_{WD} and radius R_{WD} is captured by a BH of mass M_{BH} and dimensionless spin parameter a_{spin} , most likely as a result of dynamical scattering within its host stellar system. After capture, the WD settles onto an eccentric bound orbit and undergoes a sequence of partial tidal disruption events. During each pericenter passage, a fraction of the WD mass is stripped, remains gravitationally bound to the BH, and is ultimately accreted, while the stellar core survives and continues on a bound orbit. Such repeating partial tidal disruptions have been demonstrated in previous studies (e.g., I. Zalamea et al. 2010; M. MacLeod et al. 2014; J.-H. Chen et al. 2023; J.-P. Chen et al. 2025). The mass lost during a single pericenter passage can be estimated following I. Zalamea

et al. (2010) as

$$\Delta M(\beta) \approx 6.1 \left(1 - \frac{M_{\text{WD}}}{M_{\text{Ch}}}\right)^{0.67} \left(1 - \frac{1}{2\beta}\right)^{5/2} M_{\text{WD}}, \quad (1)$$

where $M_{\text{Ch}} = 1.43 M_{\odot}$ is the Chandrasekhar mass, $\beta \equiv r_{\text{T}}/r_{\text{p}}$ is the penetration factor, $r_{\text{T}} \equiv R_{\text{WD}}(M_{\text{BH}}/M_{\text{WD}})^{1/3}$ is the tidal radius, and r_{p} is the pericenter distance. For such repeated partial tidal disruptions to occur, the encounter must be sufficiently weak, requiring

$$\beta < 1. \quad (2)$$

In addition, the pericenter distance must lie outside the BH horizon in order to avoid a direct relativistic plunge,

$$r_{\text{p}} > r_{\text{h}}, \quad (3)$$

where $r_{\text{h}} \equiv r_{\text{g}} \left(1 + \sqrt{1 - a_{\text{spin}}^2}\right)$ is the radius of the event horizon of a Kerr BH with $r_{\text{g}} = GM_{\text{BH}}/c^2$. Under these conditions, the stellar core remains gravitationally bound to the BH after each passage and continues on a stable eccentric orbit. As a result, multiple partial tidal disruption events can occur before the WD is fully disrupted. Under this picture, the system naturally produces three hierarchical timescales, ~ 100 s, ~ 1 h, and ~ 1 d, which we associate with the observed properties of GRB 250702B.

2.2. Three Characteristic Timescales

2.2.1. Flare duration: viscous timescale

At each pericenter passage, the stripped material is assumed to circularize on a timescale much shorter than the orbital period, forming an accretion disk around the BH. We therefore identify the duration of an individual gamma-ray flare with the viscous timescale of this disk. The circularization radius is taken to be $r_{\text{d}} \sim 2r_{\text{p}} = 2a(1 - e)$, where a is the semi-major axis and e is the eccentricity. The viscous timescale is then given by

$$\begin{aligned} \delta t_{\text{flare}} \approx t_{\text{vis}} &= \frac{1}{h^2 \alpha} \sqrt{\frac{r_{\text{d}}^3}{GM_{\text{BH}}}} \sim \frac{1}{h^2 \alpha} \sqrt{\frac{8R_{\text{WD}}^3}{GM_{\text{WD}} \beta^3}} \\ &\sim 100 \left(\frac{\beta}{0.6}\right)^{-\frac{3}{2}} \left(\frac{h}{0.5}\right)^{-2} \left(\frac{\alpha}{0.1}\right)^{-1} \\ &\times \left(\frac{M_{\text{WD}}}{1 M_{\odot}}\right)^{-\frac{1}{2}} \left(\frac{R_{\text{WD}}}{0.01 R_{\odot}}\right)^{\frac{3}{2}} \text{ s}, \end{aligned} \quad (4)$$

where h is the disk aspect ratio, α is the viscosity parameter, and G is the gravitational constant. For fiducial accretion-disk parameters $h \sim 0.5$ and $\alpha \sim 0.1$, Eq. (4) implies that achieving the flare duration of ~ 100 s requires the disruption of a compact object, such as the WD.

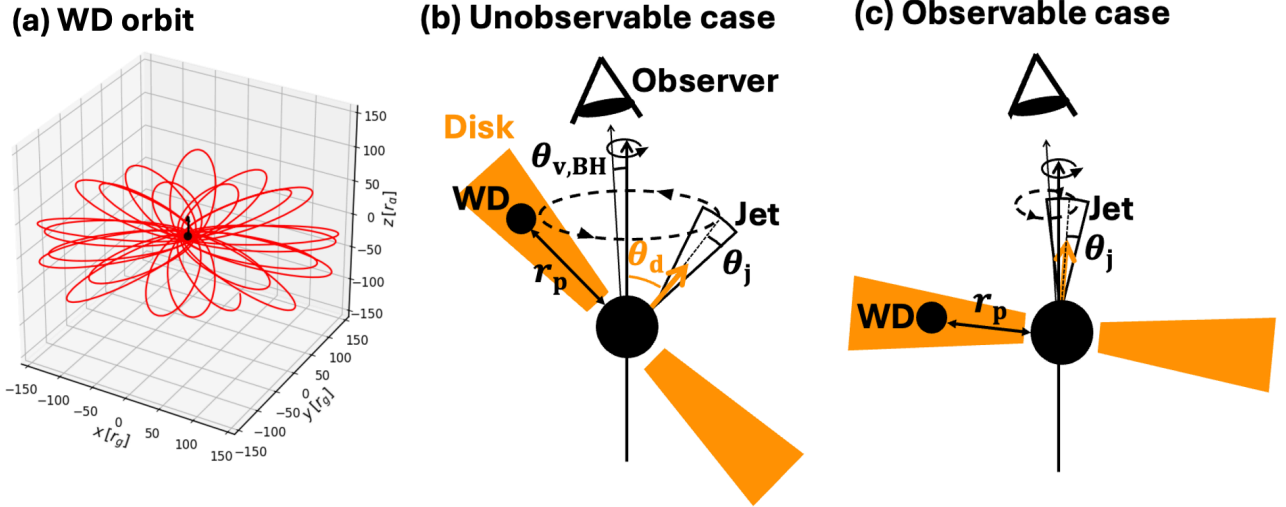


Figure 1. Our physical picture for GRB 250702B. Panel (a) shows the geodesic orbit of the WD, where the red line represents our numerical result with $a = 20 R_\odot$, $e = 0.97$, $M_{\text{BH}} = 1 \times 10^5 M_\odot$, $a_{\text{spin}} = 0.9$, and $\theta_{\text{min}} = 0.12 \text{ rad (7}^\circ\text{)}$. The BH spin axis is indicated by the vertical black line. The orbit exhibits relativistic precession. Mass loss from the WD is not included in this calculation. Panel (b) illustrates an unobservable configuration. An accretion disk forms with its angular-momentum vector tilted by an angle θ_d with respect to the BH spin axis. As a result, the jet undergoes Lense-Thirring precession. If $|\theta_{v,\text{BH}} - \theta_d| > \theta_j$, the jet does not intersect the line of sight, and the prompt emission remains unobservable. Panel (c) shows an observable configuration. If $|\theta_{v,\text{BH}} - \theta_d| \lesssim \theta_j$, the jet remains continuously observable throughout the Lense-Thirring precession.

2.2.2. Minimum flare interval: orbital period

Partial tidal disruptions occur in a nearly periodic manner, with each event taking place at pericenter passage (e.g., I. Zalamea et al. 2010; M. MacLeod et al. 2014; J.-H. Chen et al. 2023; J.-P. Chen et al. 2025). The characteristic recurrence timescale therefore corresponds to the orbital period, and we identify the minimum flare interval with

$$\Delta t_{\text{flare,min}} \simeq P_{\text{orb}} = 2\pi \sqrt{\frac{a^3}{GM_{\text{BH}}}} \sim 1 \left(\frac{a}{20 R_\odot} \right)^{\frac{3}{2}} \left(\frac{M_{\text{BH}}}{1 \times 10^5 M_\odot} \right)^{-\frac{1}{2}} \text{ h.} \quad (5)$$

To ensure that the WD can undergo many partial disruption events without the orbit shrinking significantly, the orbital evolution driven by gravitational-wave emission must be slow compared to the orbital period:

$$P_{\text{orb}} \ll \left| \frac{e}{\dot{e}} \right|_{\text{GW}}. \quad (6)$$

2.2.3. Total activity duration: secular evolution

As the WD loses mass during each pericenter passage, its orbital angular momentum decreases, leading to secular orbital evolution. The characteristic timescale for

this evolution can be estimated as

$$\delta t_{\text{tot}} \approx t_{\text{sec}} \sim \frac{M_{\text{WD}}}{\Delta M} P_{\text{orb}} \sim 1.6 \left(\frac{\Delta t_{\text{flare,min}}}{1 \text{ h}} \right) \left(\frac{\Delta M}{2 \times 10^{-2} M_\odot} \right)^{-1} \left(\frac{M_{\text{WD}}}{1 M_\odot} \right) \text{ d.} \quad (7)$$

We note that the orbital energy loss per passage is typically much smaller than the angular-momentum loss associated with each partial disruption event (e.g., I. Zalamea et al. 2010; M. MacLeod et al. 2014). Consequently, the pericenter distance remains nearly constant over many passages, consistent with recent numerical simulations (e.g., J.-H. Chen et al. 2023; J.-P. Chen et al. 2025). Since each passage removes a mass element ΔM , the total number of passages is $\simeq t_{\text{tot}}/\Delta t_{\text{flare,min}} \approx 40$. Over these successive passages, the progressive mass loss causes the WD to expand, which increases the tidal radius while the pericenter distance remains fixed. Around the ~ 40 th passage, the WD undergoes complete tidal disruption, thereby terminating the repeating flare activity.

2.3. Parameter Constraints from Observed Timescales

By combining Eqs. (4), (5), and (7) with the observed timescale of GRB 250702B, and adopting typical WD parameters of $M_{\text{WD}} \sim 1 M_\odot$ and $R_{\text{WD}} \sim 0.01 R_\odot$, together with accretion-disk parameters of $h \sim 0.5$ and

$\alpha \sim 0.1$, we obtain

$$\beta \approx 0.6 \left(\frac{\delta t_{\text{flare}}}{100 \text{ s}} \right)^{-\frac{2}{3}}, \quad (8)$$

$$\left(\frac{a}{R_{\odot}} \right)^3 \left(\frac{M_{\text{BH}}}{M_{\odot}} \right)^{-1} \approx 0.1 \left(\frac{\Delta t_{\text{flare,min}}}{1 \text{ h}} \right)^2, \quad (9)$$

$$\Delta M \approx 2 \times 10^{-2} M_{\odot} \left(\frac{\Delta t_{\text{flare,min}}}{1 \text{ h}} \right) \left(\frac{\delta t_{\text{tot}}}{1 \text{ d}} \right)^{-1}. \quad (10)$$

The inferred value of β satisfies Eq. 2. At this stage, the combination a^3/M_{BH} is constrained. Using these constraints, the eccentricity can be estimated from

$$1 - e = \frac{r_p}{a} = \frac{r_T}{a\beta} \approx 0.03 \left(\frac{\delta t_{\text{flare}}}{100 \text{ s}} \right)^{\frac{2}{3}} \left(\frac{\Delta t_{\text{flare,min}}}{1 \text{ h}} \right)^{-\frac{2}{3}}, \quad (11)$$

yielding a highly eccentric orbit with $e \approx 0.97$. Moreover, Eq. (1) gives $\Delta M(\beta \approx 0.6) \approx 2 \times 10^{-2} M_{\odot}$, consistent with Eq. (10). Finally, the orbital evolution driven by gravitational radiation satisfies Eq. (6), since the characteristic timescale $|e/\dot{e}|_{\text{GW}} \sim 100 \text{ yr}$ is much longer than the orbital period.

Using the parameters inferred above, we verify whether the system terminates after a finite number of partial disruption events. The mass-loss episodes are expected to occur periodically $\approx 1.6 \text{ d}/1 \text{ h} \approx 40$ times. After ~ 40 passages, the WD mass is expected to decrease to of order $\sim 0.1 M_{\odot}$. Using the mass-radius relation of I. Zalamea et al. (2010), $R_{\text{WD}} = 0.013 R_{\odot} \left(\frac{M_{\text{Ch}}}{M_{\text{WD}}} \right)^{1/3} \left(1 - \frac{M_{\text{WD}}}{M_{\text{Ch}}} \right)^{0.447} \sim 0.02 R_{\odot}$, the corresponding tidal radius at the 40th orbit becomes $r_T \sim 0.03 R_{\odot} \left(\frac{M_{\text{BH}}}{M_{\odot}} \right)^{1/3}$. Using the orbital parameters inferred from the observed timescales, $(a/R_{\odot})^3 (M_{\text{BH}}/M_{\odot})^{-1} \sim 0.1$, the pericenter distance is $r_p \sim 0.02 R_{\odot} \left(\frac{M_{\text{BH}}}{M_{\odot}} \right)^{1/3}$. Since $r_T > r_p$ at this stage, the WD would undergo complete tidal disruption on the ~ 40 th passage.

2.4. Jet Production and Luminosity

During each pericenter passage, a fraction of the WD mass is stripped and subsequently accreted onto the BH through an accretion disk. We assume that the accretion process launches a relativistic jet powered by the Blandford–Znajek (BZ) mechanism, which extracts rotational energy from the spinning BH via magnetic fields (R. D. Blandford & R. L. Znajek 1977). Assuming that

the jet has a half-opening angle θ_j and that the emission is approximately uniform within the jet cone, the isotropic-equivalent gamma-ray luminosity is given by

$$L_{\gamma,\text{iso}} \approx \frac{\eta_{\text{BZ}} \eta_{\text{rad}} \Delta M c^2}{\theta_j^2 \delta t_{\text{flare}}} \sim 5 \times 10^{51} \eta_{\text{BZ}} \left(\frac{\eta_{\text{rad}}}{0.1} \right) \left(\frac{\delta t_{\text{flare}}}{100 \text{ s}} \right)^{-1} \left(\frac{\Delta M}{2 \times 10^{-2} M_{\odot}} \right) \times \left(\frac{\theta_j}{0.1 \text{ rad}} \right)^{-2} \text{ erg s}^{-1}, \quad (12)$$

where η_{rad} is the radiative efficiency and η_{BZ} is the effective efficiency of the BZ jet, incorporating the effects of BH spin and accumulated magnetic flux. To reproduce the observed gamma-ray luminosity using the mass loss inferred from the observed timescales, a combined efficiency of $\eta_{\text{BZ}} \eta_{\text{rad}} \sim 0.1$ is required.

Such an efficiency implies that the BH is likely rapidly spinning ($a_{\text{spin}} \sim 1$) and that the accretion disk is in a magnetically arrested disk state. Combining Eqs. (3), (9), and (11) under the condition $a_{\text{spin}} \sim 1$ yields an upper limit on the BH mass of $M_{\text{BH}} \lesssim 10^6 M_{\odot}$, corresponding to a semi-major axis $a \lesssim 50 R_{\odot}$.

2.5. Precessing Orbits and Irregular Flare Intervals

The irregular recurrence of the observed gamma-ray flares cannot be explained solely by repeating partial disruptions occurring at each pericenter passage. We therefore attribute the irregularity to precession of the jet-launching direction.

Guided by the parameters inferred in Section 2.3, we consider the BH mass $M_{\text{BH}} \gtrsim 10^5 M_{\odot}$, corresponding to $a \gtrsim 20 R_{\odot}$ and $r_p \lesssim 3 r_g$. In this regime, the WD orbit is well approximated by a bound Kerr geodesic, which undergoes relativistic precession (see Fig. 1(a) for an illustrative example).

To reproduce the fact that only a small number of gamma-ray flares are observed, the jet must lie outside the observer's line of sight for most pericenter passages. This requires that the orbital precession angle per pericenter passage, $\theta_{\text{prec,orbit}} \gtrsim 0.1 \text{ rad} (\gtrsim 6^\circ)$, exceed the jet half-opening angle adopted in Section 2.4. Assuming a rapidly spinning BH ($a_{\text{spin}} \sim 1$), solutions of the Kerr geodesic equations indicate that such precession is achieved for prograde orbits with the minimum polar angle of the Kerr geodesic measured from the BH equatorial plane $\theta_{\text{min}} \gtrsim 0.12 \text{ rad} (\theta_{\text{min}} \gtrsim 7^\circ)$. Although our geodesic calculations neglect mass loss, this has little impact at early times, when the WD orbit is largely unaffected by mass loss.

We assume that the accretion disk formed after each pericenter passage lies in the same plane as the WD orbit at pericenter, so that the disk angular-momentum

vector is aligned with that of the WD. As a result, the disk (and the associated jet) is misaligned with respect to the BH spin axis by an angle θ_d . Such a misaligned disk experiences a Lense–Thirring torque, causing the disk and the associated jet to precess around the BH spin axis (e.g., J. C. B. Papaloizou & D. N. C. Lin 1995; P. C. Fragile et al. 2007; M. Liska et al. 2018; W. Lu et al. 2024). Based on the mass-loss rate estimated in Section 2.3, the accretion disk is expected to be in the super-Eddington regime, in which the misalignment between the disk–jet system and the BH spin axis can persist over timescales much longer than the Lense–Thirring precession timescale (e.g., A. Franchini et al. 2016; J. J. Zanazzi & D. Lai 2019). The Lense–Thirring precession timescale is given by W. Lu et al. (2024) as $t_{\text{prec,LT}} \gtrsim 100 (r_{\text{in}}/r_g)(M_{\text{BH}}/10^5, M_{\odot})$ s, which is comparable to or longer than the observed duration of a single gamma-ray flare (~ 100 s). This implies that the jet orientation can change by a non-negligible fraction of a precession cycle during a single flare. Therefore, the disk–jet system continues to undergo Lense–Thirring precession during an individual flare, with the jet sweeping out a cone of θ_d around the BH spin axis.

Here we define $\theta_{v,\text{BH}}$ as the viewing angle measured from the BH spin axis. During the Lense–Thirring precession cycle, the instantaneous angle between the jet axis and the line of sight varies between $|\theta_{v,\text{BH}} - \theta_d|$ and $\theta_{v,\text{BH}} + \theta_d$. If $|\theta_{v,\text{BH}} - \theta_d| > \theta_j$, the jet is never observable (see Fig. 1(b)). In contrast, if $\theta_{v,\text{BH}} + \theta_d \lesssim \theta_j$, the jet remains within the line of sight throughout the Lense–Thirring precession cycle and is therefore continuously observable (see Fig. 1(c)). This observability condition therefore requires that the viewing angle measured from the BH spin axis be small compared to the jet half-opening angle.

3. AFTERGLOW EMISSION

In the previous section, we consider that the WD can launch up to 40 jets over the entire sequence (hereafter, the maximum case). Most of these jets are initially viewed off-axis by the observer. As a result, the early-time emission is dominated by the four jets that happen to be launched nearly along the line of sight, while the remaining ≈ 36 jets are initially invisible. As the jets decelerate, relativistic beaming weakens, allowing these off-axis jets to become visible to the observer (e.g., J. Granot et al. 2002). Their emission can therefore brighten at late times, particularly in the radio band (e.g., D. Lazzati et al. 2018; Y. Sato et al. 2021, 2023). On the other hand, only four gamma-ray flares have been observed. This may indicate that only four jets

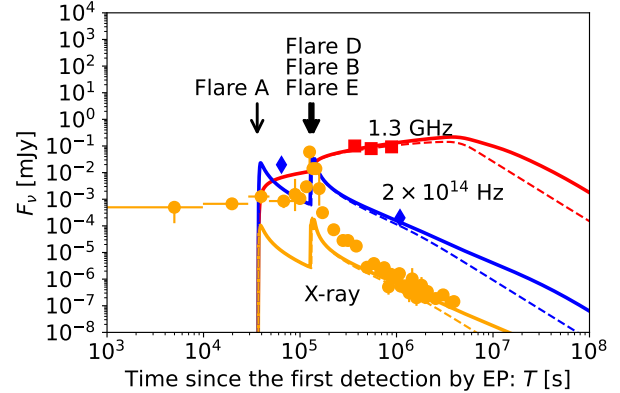


Figure 2. Afterglow light curves in the X-ray (5 keV; orange), near-infrared (2×10^{14} Hz; blue), and radio (1.3 GHz; red) bands, compared with the observed data of GRB 250702B (X-ray: orange circles; near-infrared: blue diamonds; radio: red squares). The thick solid and thin dashed lines denote the predicted emission for the maximum (40 jets) and minimum (4 jets) cases, respectively. Black arrows indicate the times of the observed gamma-ray flares.

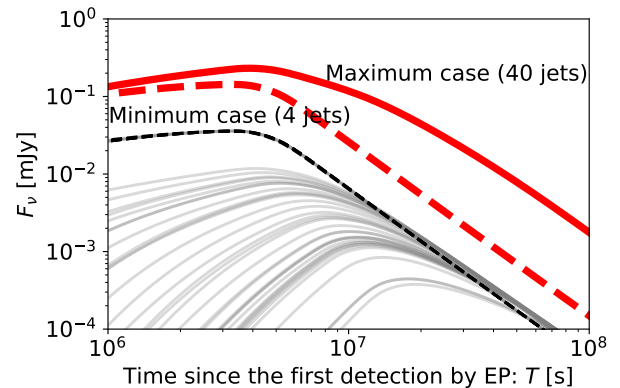


Figure 3. Predicted radio (1.3 GHz) afterglow light curves for the maximum (40 jets; red solid line) and minimum (4 jets; red dashed line) cases. The gray solid lines show the emission from individual jets in the maximum case, while the black dashed lines represent the emission from individual jets in the minimum case. At $T \sim 10^8$ s, the maximum case is approximately an order of magnitude brighter than the minimum case.

were launched in total (hereafter referred to as the minimum case), possibly as a consequence of disk instabilities (J. Granot et al. 2025) and/or choked jet scenarios (W. Lu et al. 2024). Consequently, the maximum and minimum cases are expected to exhibit distinct late-time radio afterglow behaviors. In the following, we compare these two scenarios using their predicted afterglow emission.

In the maximal case, we assume that jets are launched sequentially, one every hour, corresponding to the orbital period. For simplicity, the jet axis is assumed to

remain fixed during the afterglow phase of each episode. The total afterglow emission is computed as the sum of the radiation from 40 jets with randomly assigned viewing angles between 0 and $\pi/2$. In the minimal case, jets are launched only at the times when gamma-ray flares are observed, and all jets are assumed to be viewed on-axis.

We compute the multiwavelength afterglow emission from a single top-hat jet using the `VegasAfterglow` code (Y. Wang et al. 2025). The jet is characterized by an initial half-opening angle θ_0 , bulk Lorentz factor Γ_0 , and isotropic-equivalent kinetic energy $E_{\text{iso,K}}$. It propagates into an external medium with a power-law density profile $n(r) = A_*(r/r_0)^{-k}$, where $r_0 = 10^{17}$ cm, and produces synchrotron radiation from external shocks. We assume a power-law electron energy distribution with index p . The microphysical parameters ϵ_e , ϵ_B , and f_e denote the fractions of internal energy in nonthermal electrons and magnetic fields, and the fraction of accelerated electrons, respectively, and are taken to be constant. The emission is calculated for a viewing angle $\theta_{\text{v,jet}}$.

We present our modeling of the multiwavelength afterglow emission in the X-ray (5 keV), near-infrared (2×10^{14} Hz), and radio (1.3 GHz) bands, and compare the results with observations of GRB 250702B. The X-ray data are taken from D. Y. Li et al. (2025) and B. O'Connor et al. (2025). We convert the observed 0.3–10 keV energy flux to a flux density at 5 keV, assuming a photon index of 1.8 during the slow-cooling phase. The near-infrared data are from A. J. Levan et al. (2025) and J. Carney et al. (2025). We adopt a V-band extinction of $A_V = 4.2$ mag (B. P. Gompertz et al. 2025) and apply the corresponding extinction correction at 2×10^{14} Hz using a standard extinction law. The radio data are taken from J. Carney et al. (2025).

In order to reproduce the observed multiwavelength afterglow light curves, we adopt the following model parameters: $\theta_0 = 0.1$ rad (6°), $E_{\text{iso,K}} = 4 \times 10^{54}$ erg, $\Gamma_0 = 100$, $k = 1.0$, $A_* = 0.1$, $p = 2.6$, $\epsilon_e = 10^{-2}$, $\epsilon_B = 10^{-5}$, and $f_e = 0.1$. Figure 2 presents the resulting multiwavelength emission. In both the maximum and minimum scenarios, the early afterglow is dominated by the same four jets viewed nearly on-axis, and therefore the early X-ray and near-infrared behavior is similar in both cases. The calculated X-ray light curve exhibits two pronounced flares between $\sim 4.2 \times 10^4$ s and $\sim 1.2 \times 10^5$ s, each corresponding to the transition of an on-axis jet from the coasting phase to the self-similar adiabatic expansion stage (R. Sari 1997). The near-infrared light curve also shows two peaks, though with a different physical origin: each peak appears when the

typical synchrotron frequency ν_m of the jet component crosses the observing band. Because jets are launched at different epochs, these peaks overlap in the observer frame and produce the sequence of rapidly rising and decaying flares in both X-ray and near-infrared bands.

At later times, jets that were initially viewed off-axis in the maximum case decelerate sufficiently to become effectively on-axis (J. Granot et al. 2002). For $T \gtrsim 10^6$ s, the light curves of the maximum case therefore deviate from those of the four-jet configuration, as the off-axis jets begin to satisfy the condition $1/\Gamma \sim \theta_{\text{v,jet}} - \theta_j$ and enter the observer's line of sight, enhancing the radio emission. This behavior is illustrated by the gray solid lines in Fig. 3, where each radio peak corresponds to the passage of the typical synchrotron frequency ν_m through 1.3 GHz. By $T \sim 10^8$ s, all jets have entered the Newtonian phase and can be regarded as effectively on-axis. The radio flux from the full jet population in the maximum case is then about an order of magnitude higher than that from the four-jet configuration. Because the microphysical parameters A_* , ϵ_e , ϵ_B , and f_e are identical in both scenarios, the late-time radio emission reflects the total kinetic energy, $N_{\text{jet}} E_{\text{iso,K}} \theta_0^2 / 2$, where N_{jet} is the number of jets. At this epoch, ν_m lies below the radio band while the cooling frequency ν_c lies between the radio and near-infrared bands. The flux therefore scales as $F_\nu \propto E_{\text{iso,K}}^{\frac{6+10p-k(5+p)}{4(5-k)}} A_*^{\frac{19-5p}{4(5-k)}} \epsilon_B^{\frac{p+1}{4}} \epsilon_e^{p-1} f_e^{2-p} \sim E_{\text{iso,K}}^{1.5} A_*^{0.4} \epsilon_B^{0.9} \epsilon_e^{1.6} f_e^{-0.6}$. This scaling predicts the flux ratio of $(40/4)^{1.5} \sim 30$ between the maximum and minimum cases, consistent with our numerical results and yielding an order-of-magnitude difference in the radio flux at $T \sim 10^8$ s. At such late times, differences in jet launching epochs become negligible.

4. SUMMARY & DISCUSSION

We have shown that the hierarchical timescales observed in the prompt emission of GRB 250702B can be explained by repeating partial tidal disruptions of the WD by the BH on a highly eccentric orbit ($e \approx 0.97$). For the rapidly spinning BH with $M_{\text{BH}} \sim 10^5\text{--}10^6 M_\odot$ and $a_{\text{spin}} \sim 1$, Kerr geodesics with the semi-major axis of $a \sim 20\text{--}50 R_\odot$ and the minimum polar angle measured from the BH equatorial plane of $\theta_{\text{min}} \gtrsim 0.12$ rad ($\gtrsim 7^\circ$) undergo relativistic orbital precession, with the per-orbit precession angle exceeding the jet half-opening angle. This leads to changes in the jet direction between successive pericenter passages, explaining the irregular flare intervals. In our model, up to ≈ 40 jets are launched during the sequence of partial disruptions, but only four are initially viewed on-axis and detected as prompt gamma-ray flares. The remaining ≈ 36 jets are initially off-axis and invisible at early times, but their cumulative contri-

bution enhances the late-time radio afterglow by about an order of magnitude, providing a testable signature of orbital precession in the WD–IMBH system.

The last three flares appear relatively clustered. Since the observer is located near the BH spin axis, mass loss during the late-stage passages may have gradually aligned the WD’s orbit with the BH’s equatorial plane. Once this configuration was established, orbital precession may have been suppressed, which could have kept the jet direction nearly constant from one pericenter passage to the next.

To account for the observed gamma-ray luminosity, a magnetic field strength of $B_{\text{H}} \sim 1 \times 10^{10} a_{\text{spin}} (L_{\gamma, \text{iso}} / 5 \times 10^{51} \text{ erg s}^{-1})^{\frac{1}{2}} (\theta_{\text{j}} / 0.1 \text{ rad}) (M_{\text{BH}} / 1 \times 10^5 M_{\odot})^{-1} (\kappa / 0.06)^{-\frac{1}{2}} \text{ G}$ is required at the BH horizon, where κ is a dimensionless coefficient appearing in the BZ formula (A. Tchekhovskoy et al. 2010, 2011). However, the magnetic field supplied by the WD material is expected to be much weaker, $B_{\text{adv}} \sim 2 \times 10^5 (B_{\text{WD}} / 10^9 \text{ G}) (R_{\text{WD}} / 0.01 R_{\odot})^2 (M_{\text{BH}} / 1 \times 10^5 M_{\odot})^{-2} (\xi / 0.1) \text{ G}$, where B_{WD} is the surface magnetic field of the WD and ξ is the efficiency with which the WD magnetic field is transported to the BH horizon. This field strength is insufficient to power the jet. Therefore, an additional magnetic-field amplification mechanism, such as a dynamo process, would be necessary (e.g. J. H. Krolik & T. Piran 2011; A. Tchekhovskoy et al. 2014).

Our calculated early X-ray afterglow between $\sim 10^4$ s and $\sim 10^5$ s does not reproduce the observed behavior (see Fig. 2). The observed X-ray flux brightens on a timescale of about one day, peaks around the time of flare B, and then fades on the comparable timescale. Such day-scale variability is difficult to explain with the

afterglow component. Instead, it may arise from prompt emission associated with multiple jets viewed off-axis. In the off-axis viewing scenario, relativistic Doppler effects reduce the observed photon energy and dilate the observed timescale, producing smoother and longer-lasting variability than an on-axis jet.

Our early near-infrared afterglow light curve also shows significant variability. If detected by optical facilities such as the Zwicky Transient Facility or the Vera C. Rubin Observatory, such variability would provide independent evidence for repeating partial tidal disruptions.

If our model is correct, this event implies the rapidly rotating IMBH ($M_{\text{BH}} \sim 10^5 M_{\odot}$, $a_{\text{spin}} \sim 1$) hosting the WD on the highly eccentric orbit. Despite large uncertainties in their event rate (e.g., M. MacLeod et al. 2014; C. S. Ye et al. 2023), such systems are promising sources of low-frequency gravitational waves for space-based detectors such as the Laser Interferometer Space Antenna (e.g., P. Amaro-Seoane et al. 2023). Future multi-messenger observations may constrain the BH mass and spin, the orbital evolution, and enable tests of general relativity.

ACKNOWLEDGEMENTS

We thank Akihiro Inoue, Jim Fuller, Koki Kin, Yuki Kudoh, Tomoya Suzuguchi, and Kengo Tomida for valuable comments. This research was partially supported by JSPS KAKENHI Grant Nos. 25KJ0010 (YS), 24K17088 (TM), 22H00130, 23H04899, and 24K00668 (KK).

REFERENCES

Amaro-Seoane, P., Andrews, J., Arca Sedda, M., et al. 2023, Living Reviews in Relativity, 26, 2, doi: [10.1007/s41114-022-00041-y](https://doi.org/10.1007/s41114-022-00041-y)

Beniamini, P., Perets, H. B., & Granot, J. 2025, arXiv e-prints, arXiv:2509.22779, doi: [10.48550/arXiv.2509.22779](https://doi.org/10.48550/arXiv.2509.22779)

Blandford, R. D., & Znajek, R. L. 1977, MNRAS, 179, 433, doi: [10.1093/mnras/179.3.433](https://doi.org/10.1093/mnras/179.3.433)

Burrows, D. N., Kennea, J. A., Ghisellini, G., et al. 2011, Nature, 476, 421, doi: [10.1038/nature10374](https://doi.org/10.1038/nature10374)

Carney, J., Andreoni, I., O’Connor, B., et al. 2025, arXiv e-prints, arXiv:2509.22784, doi: [10.48550/arXiv.2509.22784](https://doi.org/10.48550/arXiv.2509.22784)

Chen, J.-H., Shen, R.-F., & Liu, S.-F. 2023, ApJ, 947, 32, doi: [10.3847/1538-4357/acfb6](https://doi.org/10.3847/1538-4357/acfb6)

Chen, J.-P., Shen, R.-F., & Chen, J.-H. 2025, arXiv e-prints, arXiv:2510.27399, <https://arxiv.org/abs/2510.27399>

Eyles-Ferris, R. A., King, A., Starling, R. L., et al. 2025, arXiv e-prints, arXiv:2509.22843, doi: [10.48550/arXiv.2509.22843](https://doi.org/10.48550/arXiv.2509.22843)

Fragile, P. C., Blaes, O. M., Anninos, P., & Salmonson, J. D. 2007, ApJ, 668, 417, doi: [10.1086/521092](https://doi.org/10.1086/521092)

Franchini, A., Lodato, G., & Facchini, S. 2016, MNRAS, 455, 1946, doi: [10.1093/mnras/stv2417](https://doi.org/10.1093/mnras/stv2417)

Gompertz, B. P., Levan, A. J., Laskar, T., et al. 2025, arXiv e-prints, arXiv:2509.22778, doi: [10.48550/arXiv.2509.22778](https://doi.org/10.48550/arXiv.2509.22778)

Granot, J., Panaiteescu, A., Kumar, P., & Woosley, S. E. 2002, ApJL, 570, L61, doi: [10.1086/340991](https://doi.org/10.1086/340991)

Granot, J., Perets, H. B., Gill, R., Beniamini, P., & O'Connor, B. 2025, arXiv e-prints, arXiv:2512.14847, doi: [10.48550/arXiv.2512.14847](https://doi.org/10.48550/arXiv.2512.14847)

Krolik, J. H., & Piran, T. 2011, *ApJ*, 743, 134, doi: [10.1088/0004-637X/743/2/134](https://doi.org/10.1088/0004-637X/743/2/134)

Lau, S. Y., & Yu, H. 2025, arXiv e-prints, arXiv:2506.10163, doi: [10.48550/arXiv.2506.10163](https://doi.org/10.48550/arXiv.2506.10163)

Lazzati, D., Perna, R., Morsony, B. J., et al. 2018, *PhRvL*, 120, 241103, doi: [10.1103/PhysRevLett.120.241103](https://doi.org/10.1103/PhysRevLett.120.241103)

Levan, A. J., Tanvir, N. R., Cenko, S. B., et al. 2011, *Science*, 333, 199, doi: [10.1126/science.1207143](https://doi.org/10.1126/science.1207143)

Levan, A. J., Martin-Carrillo, A., Laskar, T., et al. 2025, arXiv e-prints, arXiv:2507.14286, doi: [10.48550/arXiv.2507.14286](https://doi.org/10.48550/arXiv.2507.14286)

Li, D. Y., Yang, J., Zhang, W. D., & the Einstein Probe collaborations. 2025, arXiv e-prints, arXiv:2509.25877, doi: [10.48550/arXiv.2509.25877](https://doi.org/10.48550/arXiv.2509.25877)

Liska, M., Hesp, C., Tchekhovskoy, A., et al. 2018, *MNRAS*, 474, L81, doi: [10.1093/mnrasl/slx174](https://doi.org/10.1093/mnrasl/slx174)

Lu, W., Matsumoto, T., & Matzner, C. D. 2024, *MNRAS*, 533, 979, doi: [10.1093/mnras/stae1770](https://doi.org/10.1093/mnras/stae1770)

MacLeod, M., Goldstein, J., Ramirez-Ruiz, E., Guillochon, J., & Samsing, J. 2014, *ApJ*, 794, 9, doi: [10.1088/0004-637X/794/1/9](https://doi.org/10.1088/0004-637X/794/1/9)

Neights, E., Burns, E., Fryer, C. L., et al. 2025, arXiv e-prints, arXiv:2509.22792, doi: [10.48550/arXiv.2509.22792](https://doi.org/10.48550/arXiv.2509.22792)

O'Connor, B., Gill, R., DeLaunay, J., et al. 2025, arXiv e-prints, arXiv:2509.22787, doi: [10.48550/arXiv.2509.22787](https://doi.org/10.48550/arXiv.2509.22787)

Oganesyan, G., Kammoun, E., Ierardi, A., et al. 2025, arXiv e-prints, arXiv:2507.18694, doi: [10.48550/arXiv.2507.18694](https://doi.org/10.48550/arXiv.2507.18694)

Papaloizou, J. C. B., & Lin, D. N. C. 1995, *ApJ*, 438, 841, doi: [10.1086/175127](https://doi.org/10.1086/175127)

Sari, R. 1997, *ApJL*, 489, L37, doi: [10.1086/310957](https://doi.org/10.1086/310957)

Sato, Y., Obayashi, K., Theodre Zhang, B., et al. 2023, *Journal of High Energy Astrophysics*, 37, 51, doi: [10.1016/j.jheap.2022.12.004](https://doi.org/10.1016/j.jheap.2022.12.004)

Sato, Y., Obayashi, K., Yamazaki, R., Murase, K., & Ohira, Y. 2021, *MNRAS*, 504, 5647, doi: [10.1093/mnras/stab1273](https://doi.org/10.1093/mnras/stab1273)

Tchekhovskoy, A., Metzger, B. D., Giannios, D., & Kelley, L. Z. 2014, *MNRAS*, 437, 2744, doi: [10.1093/mnras/stt2085](https://doi.org/10.1093/mnras/stt2085)

Tchekhovskoy, A., Narayan, R., & McKinney, J. C. 2010, *ApJ*, 711, 50, doi: [10.1088/0004-637X/711/1/50](https://doi.org/10.1088/0004-637X/711/1/50)

Tchekhovskoy, A., Narayan, R., & McKinney, J. C. 2011, *MNRAS*, 418, L79, doi: [10.1111/j.1745-3933.2011.01147.x](https://doi.org/10.1111/j.1745-3933.2011.01147.x)

Wang, Y., Chen, C., & Zhang, B. 2025, arXiv e-prints, arXiv:2507.10829, doi: [10.48550/arXiv.2507.10829](https://doi.org/10.48550/arXiv.2507.10829)

Ye, C. S., Fragione, G., & Perna, R. 2023, *ApJ*, 953, 141, doi: [10.3847/1538-4357/ace1eb](https://doi.org/10.3847/1538-4357/ace1eb)

Zalamea, I., Menou, K., & Beloborodov, A. M. 2010, *MNRAS*, 409, L25, doi: [10.1111/j.1745-3933.2010.00930.x](https://doi.org/10.1111/j.1745-3933.2010.00930.x)

Zanazzi, J. J., & Lai, D. 2019, *MNRAS*, 487, 4965, doi: [10.1093/mnras/stz1610](https://doi.org/10.1093/mnras/stz1610)

Zhang, J.-P., Wang, C.-W., Yu, Z.-H., et al. 2025, arXiv e-prints, arXiv:2509.26283, doi: [10.48550/arXiv.2509.26283](https://doi.org/10.48550/arXiv.2509.26283)